Kinetic and Steady-State Properties of Magnetron Sputter with Three-Dimensional Magnetic Field

Chae Hwa Shon, Jun Seong Park, Bong Koo Kang and Jae Koo Lee *
Pohang University of Science and Technology, Pohang 790-784, S. Korea

A kinetic code is used to simulate kinetic plasma properties in a planar magnetron system in a realistic magnetic field in two and three dimensions. We simulate the magnetron system in order to obtain various plasma characteristics and erosion profiles of a target material with these magnetic fields. Scaling formulas are used to estimate the steady-state properties of plasma particles and to reduce computation time. Variations in the geometry and the magnetic field optimize these erosion profiles and plasma characteristics. For the plasma characteristics, we also calculate the plasma temperature and the distribution function. We found that electrons are nearly Maxwellian, while ions are not, and that the electron temperature in the bulk coincides well with the experimentally measured value.

I. INTRODUCTION

Sputtering processes using DC discharge are widely used in the microelectronics industry. In particular, planar magnetron sputtering is the major method used in coating thin films. It is also used for coating large-area display panels. Taking advantage of the magnetic field, magnetron sputtering operates at low-pressure and low-voltage conditions. The applied magnetic field confines energetic electrons near the cathode. These confined electrons ionize neutral gas and form a high-density plasma near the cathode surface. The ions produced by these electrons are accelerated toward the cathode surface with high energy. The bombardment of ions not only sputter out the target material but also produce secondary electrons which maintain the discharge.

The erosion uniformity of a target is the major problem in magnetron sputtering because of the target's cost. Estimations by computer simulation reduce the experimental efforts for design optimization [1–7]. We calculate the magnetic field in various geometries using the 2D POISSON and the 3D OPERA codes [8,9], and use a PIC/MCC two-dimensional simulation code, OOPIC [10] to estimate plasma characteristics and erosion profiles. Distribution functions for plasma particles are also obtained, showing that electrons have a near-Maxwellian distribution while ions have no such distribution. For this reason, kinetic simulation is necessary to obtain more accurate results on magnetron sputtering.

In the following section, we describe the geometry and the simulation domain, and the magnetic results used as the input of the OOPIC code. The steady-state properties of plasma characteristics, the optimization of magnetron sputtering geometry, OOPIC plasma simulation results, and the velocity and the energy distribution functions are presented in §3. Summary and conclusions are given in §4.

II. GEOMETRY AND MAGNETIC FIELDS

A. Geometry and simulation domain

An actual magnetron geometry is not easy to simulate and for sake of brevity we will not describe all the components of the experimental device. Figure 1 shows a typical magnetron geometry with cathode, substrate, anode, and magnets. Usually, the cathode is negatively biased with 400-600 volts with other conductors grounded. The applied potential is 400 V and the pressure is 5 mTorr in our simulation. The magnets located below the cathode plate are assembled to form either a racetrack-type geometry or a circular one. In our case, the magnets form a bulk racetrack geometry or an assembly of small cylindrical magnets. Cooling water flows under the cathode plate. Geometric sizes are given in Fig. 1 in mm.

The simulation domain is composed of a cathode, an anode, a substrate, and wings. The gap between the cathode and the anode conductors is filled with dielectric materials. The substrate is grounded or floated. The magnetic field is calculated using the OPERA code [9], which gives a three-dimensional (3D) magnetic field. The 3D magnetic fields calculated at various racetrack positions are used as an input to the plasma simulation code, OOPIC. We calculate the magnetic fields of different geometries and compare the fields and the plasma motions (two spatial positions and three components of velocities of plasma electrons and ions in the presence of neutral atoms) using these magnetic fields. The wings located between the cathode and the substrate are used to prevent the particles from escaping from the system and contaminating the chamber wall. The gap between the substrate and the wing is filled with a dielectric material. The simulation domain is divided by x-y grids, where we calculate the fields and the force to move particles from these fields. The Monte Carlo collision (MCC) technique is used to simulate the collision process.

*E-mail address: jkl@postech.ac.kr

B. Comparison of magnetic fields

Magnets are used to confine electrons along the field lines in the magnetron sputtering system. These confined electrons ionize neutral atoms to form plasma particles. Therefore, the magnetic field distribution is important in magnetron discharge. The plasma characteristics and the target erosion profiles are closely related to the magnetic field profile. Since the magnetic field is not simple, an analytical solution of plasma motion is not usually obtained. Some efforts have been made to analyze the plasma characteristics in one-dimensional geometry under a constant magnetic field [11,12]. Usually, magnetron simulation is executed using an assumed magnetic field.

We obtain the magnetic field data from the POISSON code (two-dimensional) and the OPERA code (three-dimensional) [9]. The plasma simulation code OOPIC can use two-dimensional (2D) or three-dimensional (3D) magnetic field data. OOPIC calculates various 2D plasma characteristics and 3D velocity profiles from these data. We assume a 2D geometry at the center of the racetrack-type magnet. Therefore, the 2D magnetic field can be used to optimize the center plasma profiles. For the off-center and the curved-edge portions of the racetrack-type magnetic field, we need a 3D magnetic field simulation. Full plasma profiles for the racetrack-type magnet need a 3D plasma simulation code. Three-dimensional plasma simulation requires a supercomputer and a considerable length of time to reach the steady state. The OOPIC code can simulate two-dimensional three-velocity plasmas, is relatively fast and can easily simulate various geometries and magnetic fields.

We obtain the magnetic fields using various magnet geometries. Figure 2 shows the geometries for 3D magnet calculations. A racetrack-type magnet is frequently used in magnetron sputtering, as shown in Fig. 2(a) and 2(b). Though the magnet in Fig. 2(a) is a racetrack type, the whole magnet is composed of small cylindrical magnets. This geometry is called an assembly-type geometry. In Fig. 2(b), the magnet is composed of bulk magnets filled with magnetic materials. We also simulate a long-bar-type magnet, as shown in Fig. 2(c). This long-bar-type magnet is calculated to compare the accuracy of 2D and 3D codes. The results of field simulation at the center of each case are also shown in the figure. The long-bar magnet's length is twice that of the above two racetrack-types for comparison of 2D results. The shapes of the contour at each magnet center are similar and a quantitative comparison is shown in Fig. 3. The comparison of fields is done at the target surface and the center of the racetrack. The components of 3D magnetic fields (OPERA results) are compared with those of 2D magnetic fields (POISSON results). As shown in the figure, the behavior of directional magnetic fields is similar, which reveals that the bulk racetrack-type magnet (Fig. 2(b)) and the long-bar-type magnet (Fig. 2(c)) results coincide with 2D POISSON code results. In contrast, the results of the assembly-type magnet differ from 2D results, due to the difference in the volume of the magnets. The volume of the assembly-type magnet is smaller than that of the bulk-type magnet, the long-bar-type magnet, and the 2D magnets, thus producing smaller magnetic fields. This is verified by changing the volume of magnets. The fields decrease with decreasing volume of the magnets.

The behavior of plasma at the center of the racetrack-type magnet can be simulated with 2D magnetic fields because the z-direction magnetic field strength is zero at the center of racetrack-type magnet, as shown in Fig. 4(c). For the behavior of plasma off-center or at the edge, the 3D magnetic field is necessary. We also simulate the plasma motion at the edge and off-center to see the difference. The off-center (4 cm from the center) and the edge (10 cm from the center) magnetic fields are compared with the central magnetic fields in Fig. 4. The off-center fields are not much different from the central magnetic fields with the exception of the z-direction field. In contrast, the edge fields deviate much from the central magnetic fields. The accuracy of 3D OPERA code is verified [13] by comparing the fields at various points of the racetrack-type magnet. Though the detailed results are not shown, the calculated fields agree with the measured ones within 5%.

III. SIMULATION RESULTS

A. Steady-state property

It is not easy to reach the steady state of magnetron sputtering with simulation because it requires a large amount of computation cost. With this limitation, the steady-state was reached by 3D particle-in-cell/Monte Carlo (PIC/MCC) simulation code [1,2]. Alternatively, we adopt the method which uses scaling formulas combined with simulation. Our simulations of magnetron sputtering do not show the steady-state characteristics of the plasma, since the number of plasma particles is increasing. In order to reduce computation time, we obtain the distribution of plasma at a certain time, but not the steady state and estimate the steady-state properties from these quantities by theoretical and experimental formulas. Certain time means that the plasma profiles do not vary with time while the particle number is increasing exponentially. The example profile obtained from simulation, as shown in Fig. 5, reveals the time trace of the current profile and the normalized current profiles. Figure 5(a) is an unnormalized current density, and Fig. 5(b) is an area-normalized one (area normalization means that we equated the area below the current profile to a certain value). After the area normalization, the peak current is found to converge with time. The current profiles also converge and do not vary much. From these results, we assume that the steady-state plasma profiles agree well with the above results.

Kuwahara and Fujiyama's formula [14],

$$\bar{J}_i = \frac{4\epsilon_0}{9}\sqrt{\frac{2e}{M}}\ \frac{V_c^{3/2}}{r_e^2}, \quad (1)$$

where M is ion mass, V_c is potential, and r_e is gyro-radius, is used for the estimation of the steady-state current density and the erosion rate. The gyro-radius r_e is obtained with the magnetic field parallel to the cathode surface. The absolute value of the total current flowing to the cathode surface is calculated with the gyro-radius and the current density profiles in Fig. 5(b) are normalized by the total current. The absolute value of current density is not exact because the gyro-radius is not a fixed value for magnetron sputtering. We observe that the profiles of current density at steady state do not vary significantly.

The erosion rate is calculated from the sputtering formula [15],

$$R_{sput} = \gamma_{sput}\ \frac{\bar{J}_i}{e}\ \frac{1}{n}\ \ cm/s, \quad (2)$$

where $\gamma_{sput}(\simeq 1)$ is the yield of sputtered atoms per incident ion, and n is the atomic density of target material. The normalized current and the erosion rates obtained for the fields of Fig. 2 are shown in Fig. 6. The profiles are similar in shape. We estimate the various magnetic field effects and the geometric effects on the plasma profiles and the erosion profiles from these results, which are useful for optimizing the magnetron geometries.

B. Parameter optimization

We used the OOPIC code to optimize magnetron sputtering. Using three parameters: wing length, wing position, and magnetic field strength, various magnetic fields were calculated. First, the effect of the wing length is investigated in three cases, 20, 30, and 40 mm. In our simulation, there are no marked differences among the three cases, except that the plasma distribution shrinks as the length increases. The erosion profiles of the three cases are similar to each another. Second, we vary the wing positions as 6, 20, and 26 mm from the anode. In this case, the particle-confining area is varied according to the wing position. As the wings approach the cathode, the plasma particles are pulled to the walls, which is not good for devices because of large particle loss. There are few changes of the erosion profiles when the wing position is varied, as shown in Fig. 7. Finally, we simulate magnetron sputtering with varying magnetic field strengths. As magnetron sputtering confines electrons with magnetic field, the strength and the profile of the magnetic field affect plasma characteristics. The erosion profile broadens as the magnetic field strength increases.

C. Plasma characteristics

Plasma characteristics are obtained for various geometries and fields. The representative plasma characteristics of the center of the racetrack-type magnet are shown in Fig. 8, where the plasma particle number variation with time, the potential, the plasma density profile, and the spatial distribution are shown. The upper line represents ion number, and lower line, electron number, in Fig. 8(a). The number of electrons usually decreases initially because the electron loss to the walls and the electrode is greater than the generation of electrons by ionization. With time, the ionization overcomes the electron loss. As the magnetic fields are similar in shape and magnitude at the center and off-center (Fig. 4), the characteristics are also similar. At the edge (Fig. 9), the profiles are different from the above cases. The plasma particles converge to one straight column in the spatial profile at the edge of the racetrack.

We also conducted a moving-type sputtering simulation by moving the magnet position by 2 cm to the left of the target center. The plasma characteristics, shown in Fig. 10, are modified greatly from the stationary case (Fig. 8). There are two columns of plasma profiles in the stationary case. In the moved case, only one column remains with a broad spatial shape. Since magnetic field lines do not terminate at the cathode but end at the side walls, the electrons confined in the magnetic field lines are directed toward the side walls and attracted to the walls by electric field.

The erosion profiles of target (Figs. 6 and 7) do not coincide well with the experimental results. The peak position nearly agrees with that of the experiment, but the erosion width does not. In the erosion process, the potential and the magnetic field change in the eroded region. We simulate a pre-eroded target geometry to determine the effects of changed potential and magnetic field, and the results are shown in Fig. 11. The plasma particles penetrate into the pre-eroded region before impinging on the pre-eroded target surface. We estimate the erosion rate while changing the ion current.

D. Velocity and energy distributions

We obtain the electron and the ion velocity distributions from this OOPIC simulation [16], by calculating the particle distribution in a specified x-location. We focus on the x-direction velocity because the potential gradient is also in this direction. Figure 12 is the electron and the ion velocity distributions in the plasma bulk and at the cathode sheath (between density peak and cathode surface). Points represent simulation results and the line is a Maxwellian fitting. The electrons' distribution is Maxwellian at the bulk and in front of cathode. In contrast, ions do not have a Maxwellian distribution, as shown in Figs. 12(c) and 12(d). Many ions are located in

the high velocity tail. These results indicate that particle simulation produces results different from a fluid theory which assumes a Maxwellian distribution. Hybrid codes have been developed to improve the accuracy of a fluid code and the speed of a particle code. These are the electron fluid-ion particle hybrid model [17,18], the electron particle-ion fluid hybrid model [19], and the fluid modeling of bulk plasma [20].

To clarify particle distribution, we convert the velocity distribution to the energy distribution. Energy distribution is plotted in a semilog scale in Fig. 13. The electron energy distributions in Figs 13(a) and 13(b) form a near-straight line. Ninety percent of electrons in the bulk and the sheath have energies below 10 eV. In contrast to the electron energy distribution, the ion energy distribution in Fig. 13 is not a straight line. Ions have a non-Maxwellian distribution in the bulk and sheath, as in Figs. 12(c) and 12(d), and have two slopes in the energy distribution as in Fig. 13(c) and 13(d). In contrast to the electron energy distribution, the ion energy distribution deviates much from the Maxwellian distribution. Therefore, it is hard to fit the distribution to a Maxwellian one. There exist a steep slope in the lower energy region and mild slope in the high-energy region. This is consistent with the velocity-distribution profile. The high-energy tail of the velocity distribution corresponds to a higher ion energy distribution. In the bulk region, 90% of the ions have energies below 60 eV. In the sheath, 90% of the ions have energies below the 150 eV range. The ions are accelerated under the bulk and the sheath potential, and the maximum ion energy in the sheath approaches the applied potential of 400 V.

As it is not easy to measure low-energy particle distribution experimentally, simulation can produce results that elucidate the experimental results. The energy of ions in the tail portion is high and contributes to high sputtering and cathode erosion. Therefore, this simulation information is useful for experiments. The energy distribution of ions impinging on the cathode is crucial in determining the secondary emission of electrons as well as the sputtering and erosion rates.

We estimate the electron temperature from the Maxwellian distribution information. The slope of the electron energy distribution corresponds to the inverse of electron temperature. In the bulk, the electron temperature is about 6 eV, which is the normal bulk temperature [14,21] of a magnetron and coincides with the previously calculated plasma temperatures [16].

IV. SUMMARY AND CONCLUSION

We simulate magnetron sputtering with a kinetic code, where 2D or 3D magnetic fields are used as input. A 3D magnetic field is necessary for the plasma characteristics along the racetrack-type sputter geometry. With these magnetic fields, we simulate magnetron sputtering in various geometries for optimization.

Scaling formulas, in combination with simulation, are used to estimate the steady-state current density and the erosion rate. The wing length and the position do not affect the erosion profiles significantly. As the magnetic field strength increases, the erosion profile broadens. The distribution of plasma particles changes with varying parameters. The magnetic fields near the edge are very different from those at the center and the plasma profiles change. When the magnets are moved to the side below the target, the moved portion of the plasma densities decreases since the magnetic field strength is lower than the potential difference in the moved space. This lowered magnetic field no longer confines plasma particles.

Plasmas usually have a Maxwellian distribution in the bulk. Electrons in the magnetron sputtering simulation have the Maxwellian distribution, but the ions are non-Maxwellian in almost half of the simulation domain. Because of the low pressure, the ions are accelerated rapidly to the target. The bulk electron temperature is estimated from the velocity distribution, which coincides well with the calculated and the experimental values.

ACKNOWLEDGMENTS

The authors would like to thank Y.S. Moon of LGE for helpful discussions and suggestions. The present study was supported in part by the PDP Research Center, BSRI Project No. 98-2439 and BSRI-Special Fund.

[1] K. Nanbu, S. Segawa and S. Kondo: Vacuum **47** (1996) 1013.
[2] K. Nanbu and S. Kondo: Jpn. J. Appl. Phys. **36** (1997) 4808.
[3] S. Ido and K. Nakamura: Jpn. J. Appl. Phys. **32** (1993) 5698.
[4] S. Ido and K. Nakamura: Jpn. J. Appl. Phys. **35** (1996) 2302.
[5] S. Ido, T. Suzuki and M. Kashiwagi: Jpn. J. Appl. Phys. **37** (1998) 965.
[6] E. Shidoji, M. Nemoto, T. Nomura and Y. Yoshikawa: Jpn. J. Appl. Phys. **33** (1994) 4281.
[7] T. Kobayashi, K. Itagaki, T. Uchiyama, T. Tsukada and N. Hosokawa: Proc. 3rd Int. Symp. Sputtering and Plasma Processes, June, 1995, Tokyo, p. 23.
[8] J.H. Billen and L.M. Young: Poisson Superfish (Los Alamos National Laboratory, 1997).
[9] OPERA-3d Reference Manual (Vector Fields Limited, Oxford, 1994).
[10] J. P. Verboncoeur, A. B. Langdon and N. T. Gladd: Comp. Phys. Commun. **87** (1995) 199.
[11] N. F. Cramer: J. Phys. D: Appl. Phys. **30** (1997) 2573.

[12] J. W. Bradley: Plasma Sources Sci. Technol. **5** (1996) 622.
[13] Y. S. Moon: private communication.
[14] K. Kuwahara and H. Fujiyama: IEEE Trans. Plasma Sci. **22** (1994) 442.
[15] M. A. Lieberman and A. J. Lichtenberg: Principles of plasma discharges and materials processing (John Wiley and Sons, Inc, New York, 1994) p. 522.
[16] C. H. Shon, J. K. Lee, H. J. Lee, Y. K. Shin, Y. Yang and T. H. Chung: IEEE Trans. Plasma Sci. **26** (1998) 1635.
[17] R. K. Porteous and D.B. Graves: IEEE Trans. Plasma Sci. **19** (1991) 204.
[18] R. K. Porteous, H-M Wu, and D. B. Graves: Plasma Sources Sci. Technol. **3** (1993) 25.
[19] Y. K. Shin, C. H. Shon, H. S. Lee, W. Kim, and J. K. Lee: Proc. of the 18th Int. Display Research Conf. Asia Display '98, Seoul, 1998, p. 609.
[20] R. Krimke and H. M. Urbassek: Plasma Sources Sci. Technol. **5** (1996) 389.
[21] S. M. Rossnagel and H. R. Kaufman: J. Vac. Sci. & Technol. **A4** (1986) 1822.

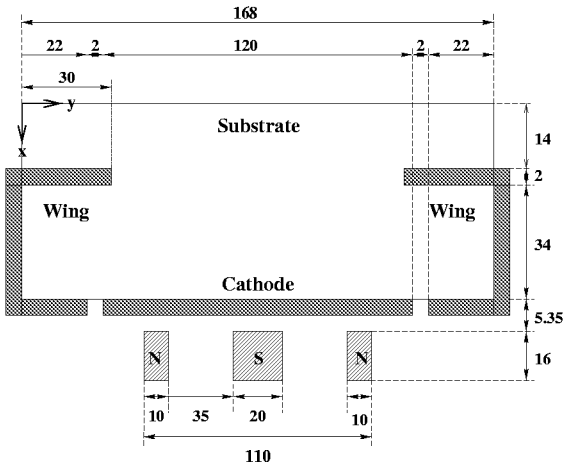

FIG. 1. Schematic diagram of the magnetron sputtering system used in the simulation.

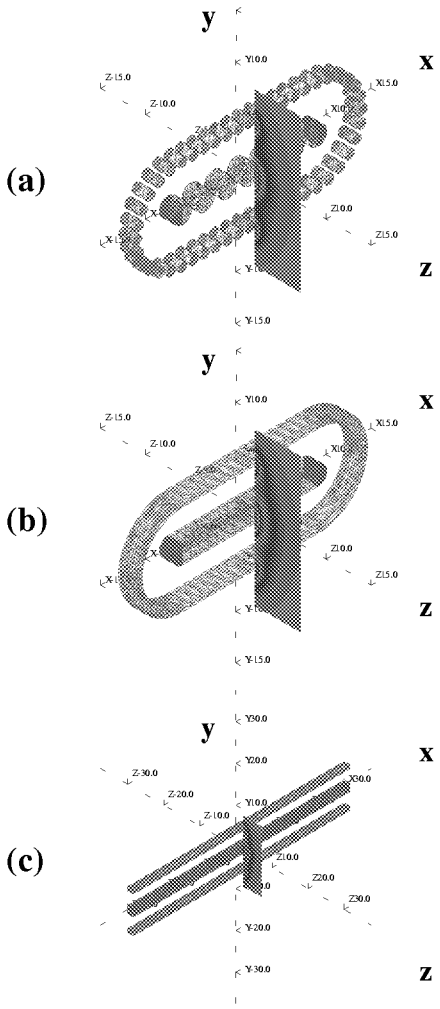

FIG. 2. The 3D geometry of (a) an assembly of small cylindrical magnets for a racetrack (assembly-type magnet), (b) a bulk racetrack-type (bulk-type magnet), and (c) a long-bar-type magnet.

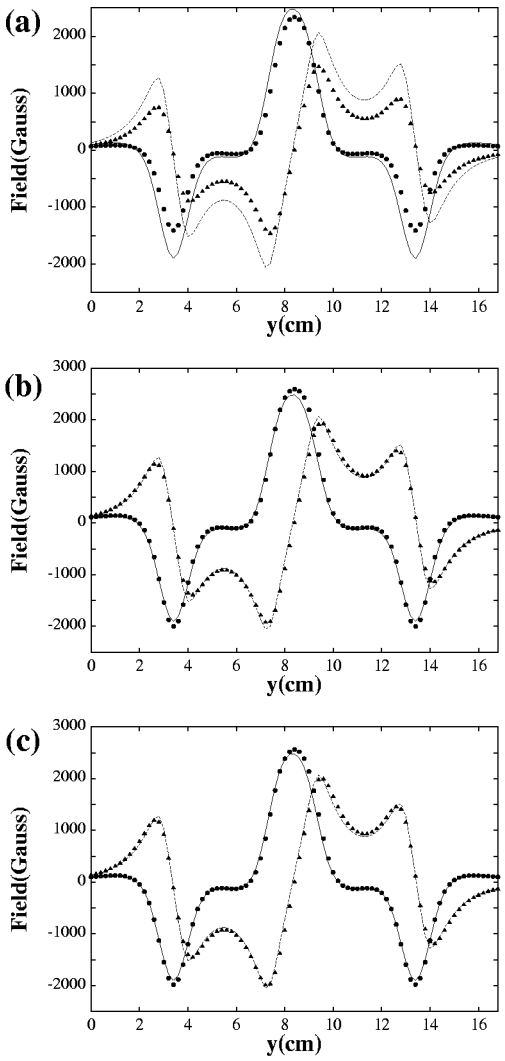

FIG. 3. Comparison of the 2D magnetic field strengths on the target with 3D fields of (a) an assembly-type magnet, (b) a bulk-type magent, and (c) a long-bar-type magnet at the center of racetrack. •: Bx components of assembly type, ▲: By components of bulk type, solid line: Bx components of 2D fields, dashed line: By components of 2D fields.

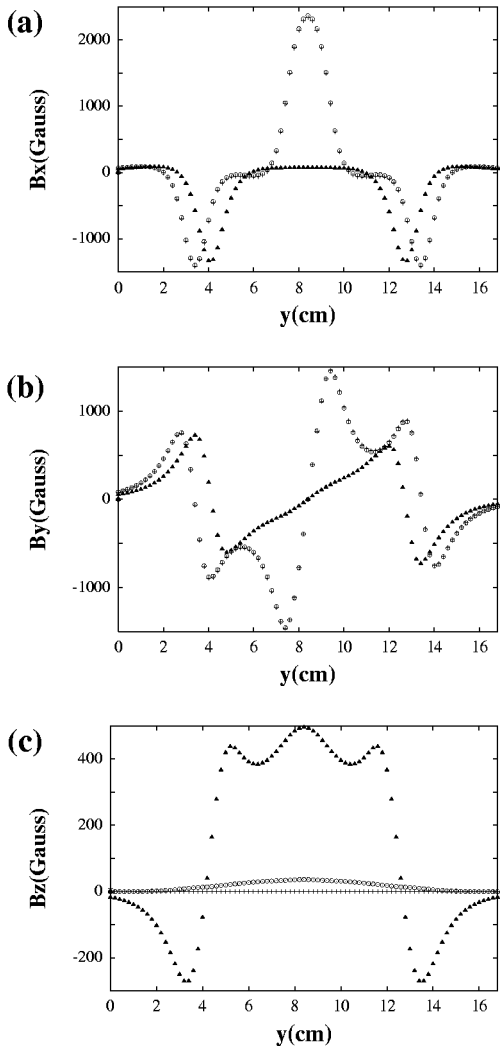

FIG. 4. Magnetic field of the assembly-type magnet at three different positions of (a) Bx, (b)By, and (c)Bz. +: at center, o: 4 cm from the center (off-peak), ▲: 10 cm from the center (edge).

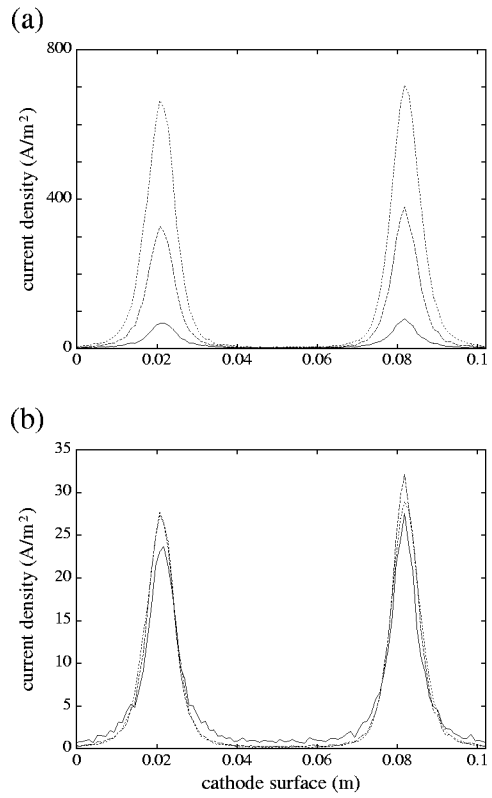

FIG. 5. (a) Current density and (b) current density normalized by Kuwahara and Fujiyama's formula at the cathode at three different times. Solid line: 2 μs, dashed line: 3 μs, dotted line: 4 μs.

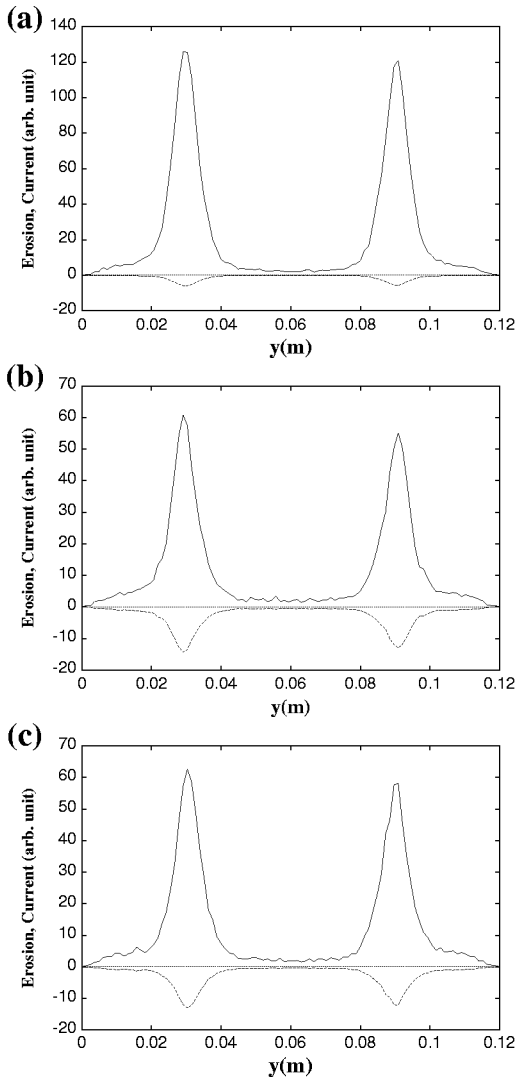

FIG. 6. Erosion and current density of (a) an assembly-type magnet, (b) a bulk-type magnet, and (c) a 2D magnet case in arbitrary units. Solid line: current density, dashed line: erosion profile.

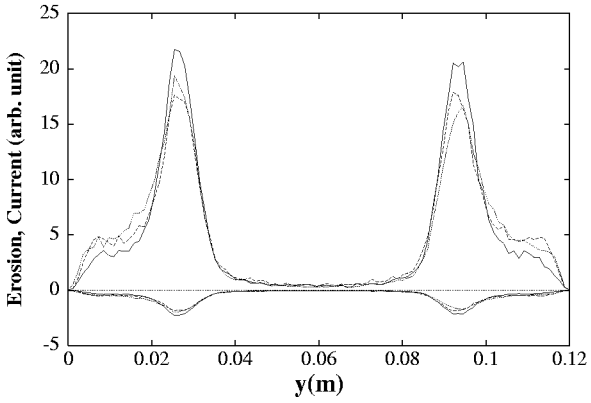

FIG. 7. Erosion and current density with varying wing positions in arbitrary units. Solid line: 6 mm, dashed line: 20 mm, dotted line: 26 mm from anode.

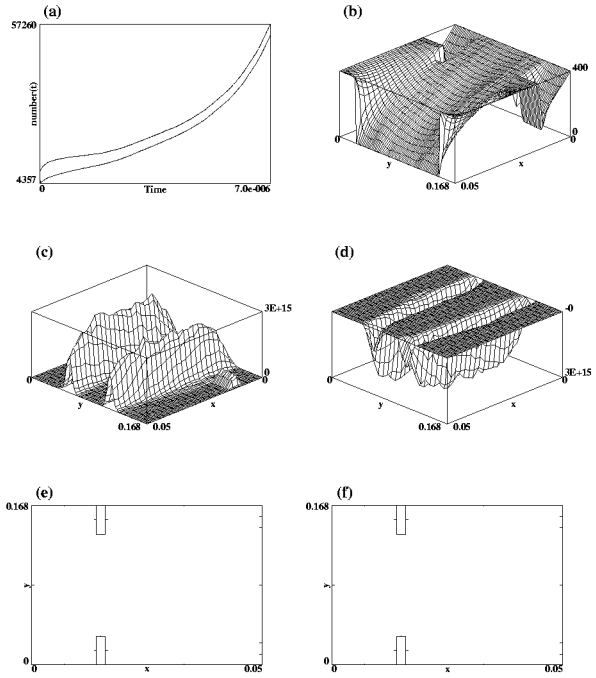

FIG. 8. Simulation results of the assembly-type magnet at the magnet's center. (a) Total number density, where upper line is ion number and lower line is electron number, (b) electric potential, (c) Ar ion number density, (d) electron number density, (e) Ar ion distribution, and (f) electron distribution in x-y space.

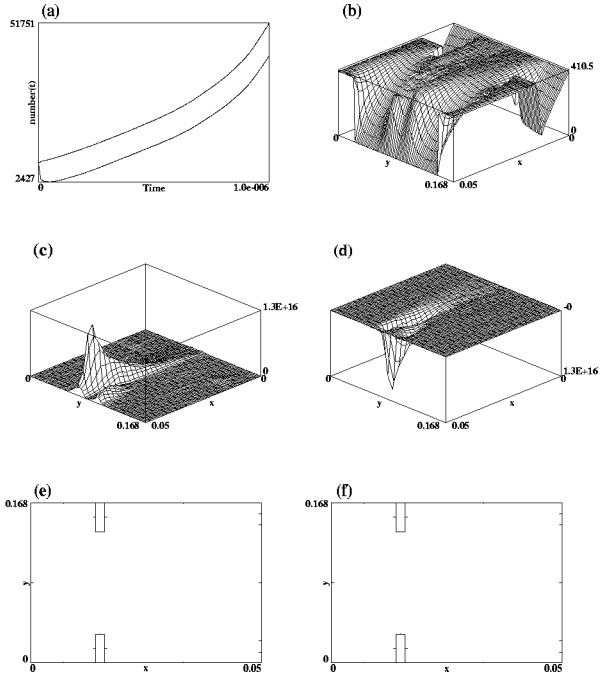

FIG. 9. Simulation results of the assembly-type magnet at 10 cm from the center of the magnet (edge). (a) Total number density, where upper line is ion number and lower line is electron number, (b) electric potential, (c) Ar ion number density, (d) electron number density, (e) Ar ion distribution, and (f) electron distribution in x-y space.

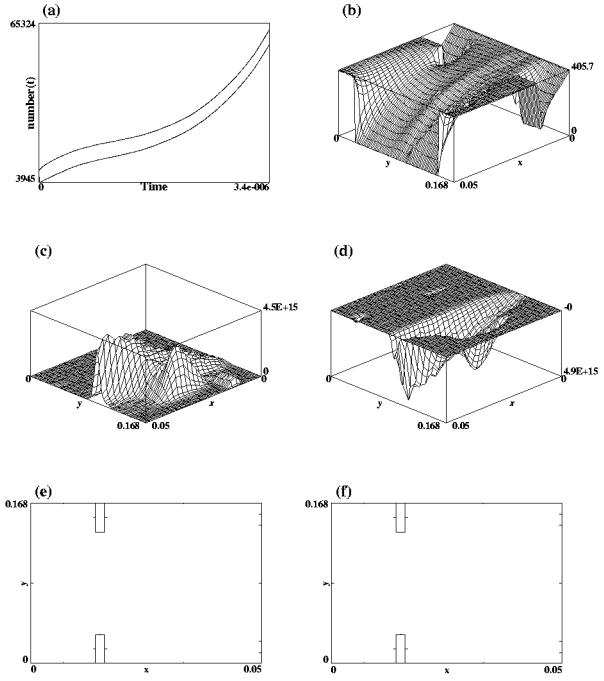

FIG. 10. Simulation results when the magnets are moved to the wall by 2 cm. (a) Total number density, where upper line is ion number and lower line is electron number, (b) electric potential, (c) Ar ion number density, (d) electron number density, (e) Ar ion distribution, and (f) electron distribution in x-y space.

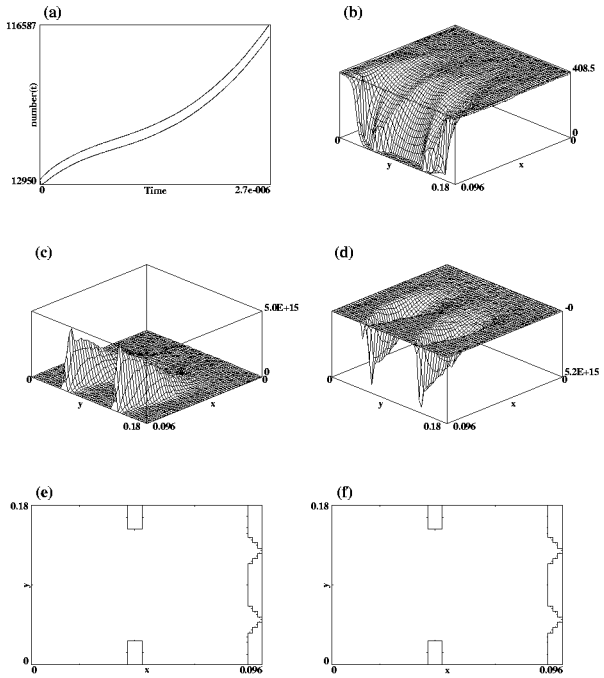

FIG. 11. Simulation results with a pre-eroded target. (a) Total number density, where upper line is ion number and lower line is electron number, (b) electric potential, (c) Ar ion number density, (d) electron number density, (e) Ar ion distribution, and (f) electron distribution in x-y space.

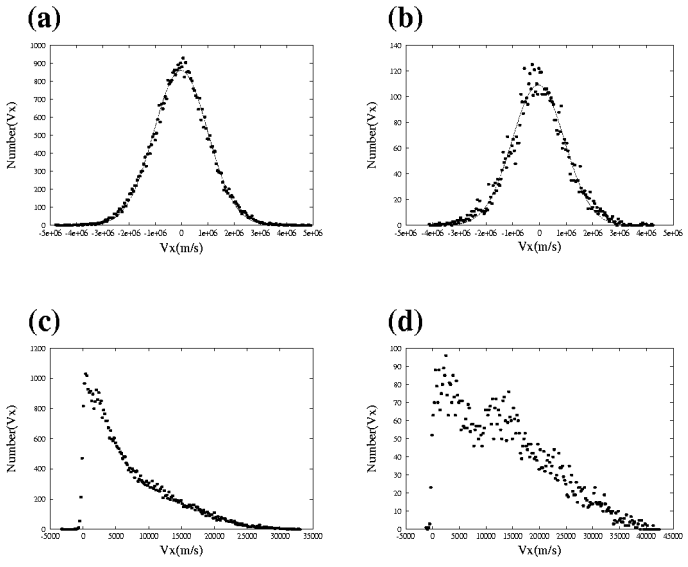

FIG. 12. The x-direction velocity distributions of (a) electrons at the bulk region, (b) electrons in front of cathode, (c) Ar ions at the bulk region, and (d) Ar ions in front of cathode.

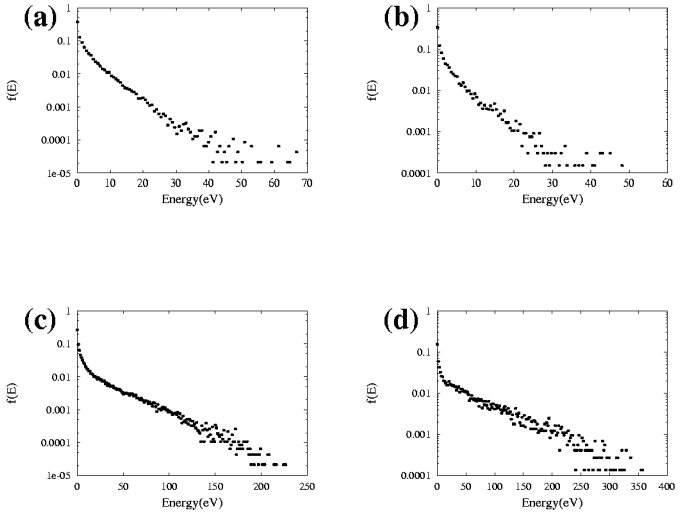

FIG. 13. The x-direction energy distribution function of (a) electrons at the bulk region, (b) electrons in front of cathode, (c) Ar ions at the bulk region, and (d) Ar ions in front of cathode.